Phosphorene Nanoribbons, Phosphorus Nanotubes, and van der Waals Multilayers

5 AUTHORS, INCLUDING:

Ning Lu
Chinese Academy of Agricultural Sciences
162 PUBLICATIONS   **2,076** CITATIONS

SEE PROFILE

Jun Dai
University of Nebraska at Lincoln
41 PUBLICATIONS   **609** CITATIONS

SEE PROFILE

Xiaojun Wu
University of Science and Technology of China
114 PUBLICATIONS   **2,338** CITATIONS

SEE PROFILE

Zeng Cheng
University of Science and Technology of China
380 PUBLICATIONS   **6,802** CITATIONS

SEE PROFILE

Phosphorene Nanoribbons, Phosphorus Nanotubes, and van der Waals Multilayers

Hongyan Guo,[†,‡,⊥] Ning Lu,[§,‡,⊥] Jun Dai,[‡] Xiaojun Wu,*[,†,∥,∇] and Xiao Cheng Zeng*[,‡,∥]

[†]CAS Key Lab of Materials for Energy Conversion, Department of Materials Science and Engineering, University of Science and Technology of China, Hefei, Anhui 230026, China

[‡]Department of Chemistry and Department of Mechanical and Materials Engineering, University of Nebraska-Lincoln, Lincoln, Nebraska 68588, United States

[§]Center for Nano Science and Technology, Department of Physics, Anhui Normal University, Wuhu, Anhui 241000, China

[∥]Hefei National Laboratory for Physical Sciences at the Microscale, University of Science and Technology of China, Hefei, Anhui 230026, China

[∇]Synergetic Innovation Center of Quantum Information & Quantum Physics, University of Science and Technology of China, Hefei, Anhui 230026, China

S *Supporting Information*

ABSTRACT: We perform a comprehensive first-principles study of the electronic properties of phosphorene nanoribbons, phosphorus nanotubes, multilayer phosphorene sheets, and heterobilayers of phosphorene and two-dimensional (2D) transition-metal dichalcogenide (TMDC) monolayer. The tensile strain and electric-field effects on electronic properties of low-dimensional phosphorene nanostructures are also investigated. Our calculations show that the bare zigzag phosphorene nanoribbons (z-PNRs) are metals regardless of the ribbon width, whereas the bare armchair phosphorene nanoribbons (a-PNRs) are semiconductors with indirect bandgaps and the bandgaps decrease with increasing ribbon width. We find that compressive (or tensile) strains can reduce (or enlarge) the bandgap of the bare a-PNRs while an in-plane electric field can significantly reduce the bandgap of the bare a-PNRs, leading to the semiconductor-to-metal transition beyond certain electric field. For edge-passivated PNR by hydrogen, z-PNRs become semiconductor with nearly direct bandgaps and a-PNRs are still semiconductor but with direct bandgaps. The response to tensile strain and electric field for the edge-passivated PNRs is similar to that for the edge-unpassivated (bare) a-PNRs. For single-walled phosphorus nanotubes, both armchair and zigzag nanotubes are semiconductors with direct bandgaps. With either tensile strains or transverse electric field, behavior of bandgap modulation similar to that for a-PNRs can arise. It is known that multilayer phosphorene sheets are semiconductors whose bandgaps decrease with an increase in the number of multilayers. In the presence of a vertical electric field, the bandgaps of multilayer phosphorene sheets decrease with increasing electric field and the bandgap modulation is more significant with more layers. Lastly, heterobilayers of phosphorene (p-type) with an n-type TMDC (MoS$_2$ or WS$_2$) monolayer are still semiconductors while their bandgaps can be reduced by applying a vertical electric field as well. We also show that the combined phosphorene/MoS$_2$ heterolayers can be an effective solar cell material. Our estimated power conversion efficiency for the phosphorene/MoS$_2$ heterobilayer has a theoretical maximum value of 17.5%.
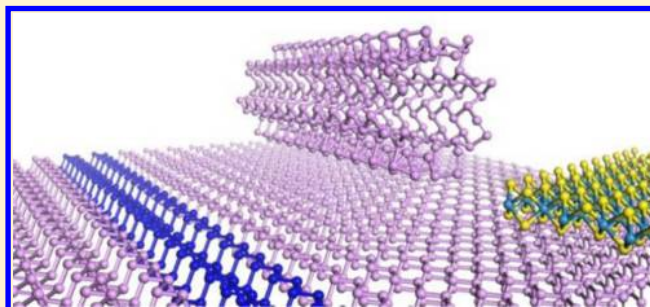
INTRODUCTION

Two-dimensional (2D) materials with atomic thickness, such as carbon graphene, boron-nitride, and 2D transition-metal dichalcogenides (TMDCs), have attracted considerable attention because of their novel properties that differ from their bulk counterparts.[1−4] Graphene is known to have some remarkable electronic and mechanical properties such as high carrier mobility, but the absence of a bandgap limits its performance in providing relatively large off current and high on−off ratio. As a representative of 2D TMDCs, MoS$_2$ monolayer possesses a direct bandgap of ~1.8 eV and relatively high on−off ratio.

However, the carrier mobility of MoS$_2$ is just several tens of square centimeters per volt-second, much lower than that of graphene.[5,6]

Recently, a new 2D material, namely, layered black phosphorus or phosphorene,[7] has been isolated in the laboratory through mechanical exfoliation from bulk black phosphorus and has immediately received considerable

attention.[7−17] It turns out that phosphorene possesses some remarkable electronic properties as well. For example, it is reported that phosphorene has the drain current modulation up to 10^5 and carrier mobility up to 1000 cm^2/(V s), which makes phosphorene a potential candidate for future nanoelectronics applications.[12] Phosphorene also has a direct bandgap which can be modified from 1.51 eV for a monolayer to 0.59 eV for a five-layer.[13] Moreover, the p-type black phosphorene transistor has already been integrated with the n-type MoS$_2$ transistor to make a 2D CMOS inverter.[17]

Tunability of electronic properties of 2D materials is crucial for their applications in nanoelectronics. Several strategies are commonly used: (1) converting a 2D sheet to 1D structure, such as 1D nanoribbons or nanotubes;[18−20] (2) varying the number of stacked 2D sheets of the same material or constructing van der Waals heterolayers by stacking different 2D materials;[20−26] and (3) applying either an external electric field (in-plane or vertical) or a tensile (or compressive) strain, which is widely used for tuning bandgaps of 2D or 1D materials.[22−24,27−38] A strain may even induce the semiconductor-to-metal transition, and strain-controlled anisotropic conductance has also been predicted for phosphorene.[10,14]

In this article, we report a systematic study of electronic properties of phosphorene nanoribbons (PNRs), single-walled phosphorus nanotubes (SW-PNTs), multilayer phosphorene sheets, and heterobilayers with a 2D TMDC sheet. Effects of external electric field or tensile strain have also been investigated. Our study suggests that low-dimensional phosphorene-based nanostructures are very versatile and either a mechanical or an electric pathway can be adopted to engineer their bandgaps and other electronic properties.

■ RESULTS AND DISCUSSION

One-Dimensional Phosphorene Nanoribbons. Figure 1 illustrates structures of PNRs with unpassivated zigzag or armchair edges or hydrogen-passivated zigzag or armchair egdes (where the periodicity is along the ribbon direction). Electronic structures of the edge-unpassivated z-PNRs with width N_z = 5−12 are computed, and all exhibit metallic
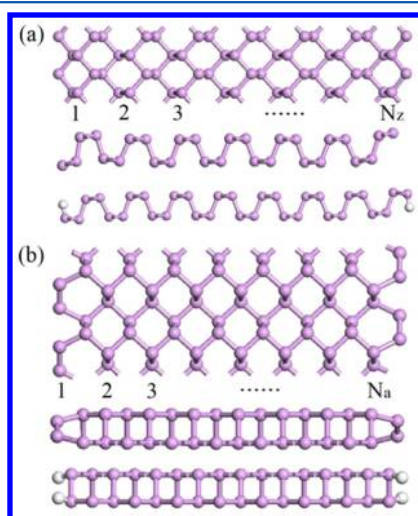
Figure 1. Structures of phosphorene nanoribbons (PNRs) with unpassivated edges (top and side views) and the H-passivated edges (side view): (a) a zigzag PNR (z-PNR) and (b) an armchair PNR (a-PNR). The purple and white spheres represent P and H atoms, respectively.

character (see Figure S1 of Supporting Information). The computed electronic structure of the edge-unpassivated 8-zigzag PNR is shown in Figure 2a, where the partial charge
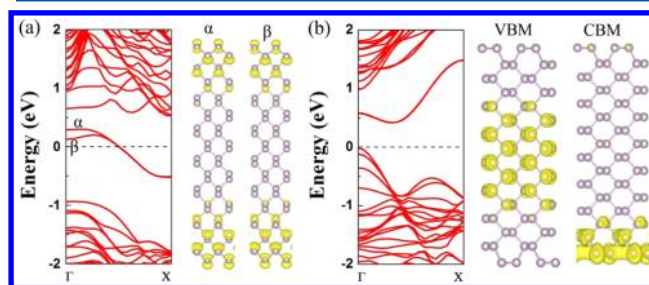
Figure 2. Computed band structures (PBE) of the edge-unpassivated (a) 8-zigzag and (b) 8-armchair PNRs. Right panels in (a) show the partial charge density distribution corresponding to the α and β bands. Right panels in (b) show the partial charge density distribution of the valence band maximum (VBM) and the conduction band minimum (CBM). The isosurface value is 0.002 e/bohr^3. The Fermi level is set to zero.

density corresponding to the α and β bands shows that the metallic character stems from the P atoms near the edges. Moreover, the partial charge density distribution corresponding to the α and β bands at the Γ point (Figure S2 of Supporting Information) indicates that there are central atoms of the PNR contributing to the β band at the Γ point but not to the α band, resulting in the splitting of α and β bands around the Γ point. As the width of the edge-unpassivated z-PNR increases, the splitting of the α and β bands decreases gradually (see Figure S1 of Supporting Information). When an in-plane electric field E_{ext} in the range of 0.1−0.5 V/Å is applied across zigzag PNRs (i.e., normal to the ribbon direction), the edge-unpassivated z-PNRs remain metallic. We have also investigated the effect of tensile strains on the electronic properties of z-PNRs and found that the strains have little effect on the band structures of the edge-unpassivated z-PNRs. Additional computation based on the HSE06 functional confirms that the edge-unpassivated z-PNRs remain metallic under the tensile strain.

Contrary to metallic character of the edge-unpassivated z-PNRs, all the edge-unpassivated a-PNRs are semiconductors with indirect bandgaps. Figure 3 shows a plot of bandgaps versus widths of the edge-unpassivated a-PNRs (see Figure S3 of Supporting Information for detailed band structures). One can see that the bandgap decreases with increasing width of a-
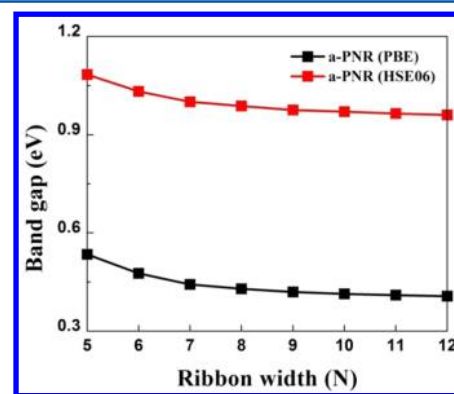
Figure 3. Variation of the bandgap of the edge-unpassivated armchair-PNRs versus their width N ($5 \leq N \leq 12$).

PNRs because of the weaker interaction between the two edges for the wider a-PNR. A 5-armchair PNR has an indirect bandgap of 0.53 eV (PBE calculation), while a 9-armchiar PNR has an indirect bandgap of 0.42 eV. Computed electronic structure of the edge-unpassivated 8-armchair PNR is shown in Figure 2b with the partial charge density corresponding to VBM and CBM, indicating that the VBM is contributed by the P atoms in the central region of the PNR while the CBM is contributed by the P atoms in the edges of the 8-armchair PNR. Here, the CBM states are degenerate because of the edge states.

Unlike the edge-unpassivated z-PNRs, the tensile strain has a significant effect on the electronic properties of the edge-unpassivated a-PNRs. As shown in Figure 4a, the bandgap of an
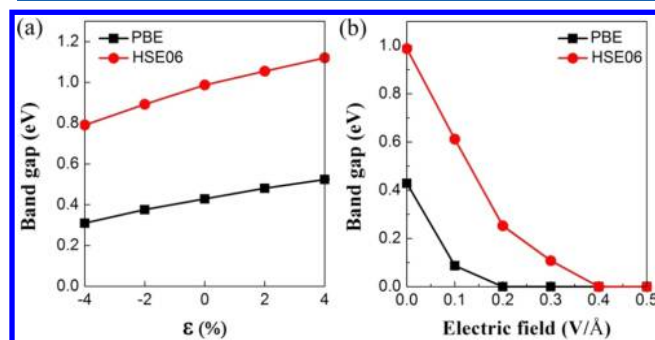

Figure 4. (a) Computed bandgaps of the edge-unpassivated 8-armchair PNR versus the tensile strain, ranging from −4% to 4%. Here, "−" represents compression and "+" represents expansion. (b) Computed band gaps versus in-plane transverse electric field for the edge-unpassivated 8-armchair PNR.

8-armchair PNR exhibits a linear response to the tensile strain, ranging from 0.31 eV at −4% compressive strain to 0.52 eV at 4% expansive strain. The HSE06 results also confirm the same trend on strain-dependent bandgap. The computed band structures corresponding to the −4% and 4% strains are plotted in Figure S4 of Supporting Information. One can see that the VBM shift is a main reason for the bandgap modification. The VBM is mainly contributed by P−P bonding states. When the P−P bond length is elongated for about 0.02 Å because of the −4% to 4% strain, the VBM is shifted by 0.17 eV. On the other hand, the CBM is mainly contributed by the edge atoms and is thus sensitive to the reconstruction of edge atoms. Hence, the tensile strain has much less effect on the CBM.

As shown in Figure 4b, the edge-unpassivated a-PNRs also exhibit significant response to the in-plane transverse electric field. Taking the 8-armchair PNR as an example, its bandgap is 0.43 eV. Under the in-plane transverse electric field of 0.1 V/Å, the bandgap is reduced to 0.10 eV. When magnitude of the electric field increases to 0.2 V/Å, the bandgap vanishes so that the 8-armchair PNR undergoes a semiconductor-to-metal transition. Further increases of the electric field do not change the metallic character of the a-PNRs. The HSE06 results are consistent with PBE results, except that the semiconductor-to-metal transition occurs under the field of 0.4 V/Å. The bandgap reduction with increasing electric field can be understood from the Stark effect.[20] Notably, charge of the PNR redistributes under the electric field, as shown in Figure S5 of Supporting Information. In particular, charge corresponding to the CBM and VBM changes in the opposite direction with changing electric field, leading to the downshift of CBM and upshift of

VBM. Figure S5 also clearly shows that the CBM is contributed by the edge state. Under the in-plane field, the two degenerate edge states are separately shifted downward and upward, leading to the splitting of the two edge states.

Besides the edge-unpassivated PNRs, electronic properties of edge H-passivated PNRs are also investigated. In stark contrast to the metallic edges of unpassivated z-PNRs, the computed results based on both PBE and HSE06 functional show that the z-PNRs with H-passivated edges exhibit nearly direct bandgaps. As shown in Figure 5a, the 8-zigzag PNR with H-passivated
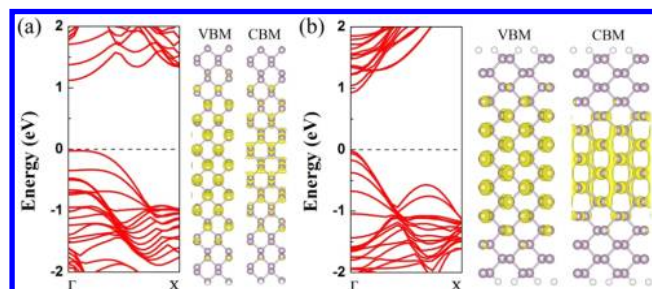

Figure 5. Computed band structures (PBE) of (a) the edge H-passivated 8-zigzag PNR and (b) the edge H-passivated 8-armchair PNR. Right panels in (a) and (b) display partial charge density distribution corresponding to VBM and CBM. The isosurface value is 0.002 e/bohr^3. The Fermi level is set to zero.

edges is a semiconductor with nearly direct bandgap of 1.14 eV (PBE) or 1.83 eV (HSE06). The partial charge density distribution corresponding to the VBM and CBM indicates that both VBM and CBM are contributed by the P atoms in the central region of the PNRs. With the hydrogen passivation, the contribution of the edge states to the Fermi level region disappears, thereby leading to the metal-to-semiconductor transition.

For the a-PNRs with H-passivated edges, the computed results based on both PBE and HSE06 functional show that all a-PNRs are still semiconductors but with direct bandgaps, compared to the indirect bandgaps for edge-unpassivated a-PNRs. Figure 5b shows the edge H-passivated 8-armchair PNR exhibits a direct bandgap of 0.94 eV (PBE). Both VBM and CBM are contributed by the P atoms in the central region of the 8-armchair PNR. Hence, we conclude that the edge passivation is the main reason for the indirect-to-direct bandgap transition.

Figure 6 shows computed bandgaps of the edge H-passivated PNRs versus their width $N = 5−12$. The bandgap decreases with increasing N because of weaker quantum confinement. Eventually, when N approaches to infinity, the bandgap of the edge H-passivated PNR should approach to that of monolayer phosphorene (1.51 eV based on HSE06). In addition, we investigate the effect of tensile strain and in-plane transverse electric field on electronic properties of the edge H-passivated PNRs. Taking the 7-PNR for an example, the computed results (see Figure S6 of Supporting Information) show that the bandgap decreases under compressive strain and increases under expansive strain, in the range of −4% to 4%. The bandgap also decreases with increasing magnitude of in-plane electric field, similar to that of the edge-unpassivated a-PNRs.

To examine relative stabilities of PNRs, we compute the cohesive energy per atom for both zigzag and armchair PNRs versus the ribbon width (see Figures S7 and S8 of Supporting Information). For the edge-unpassivated PNRs, the cohesive
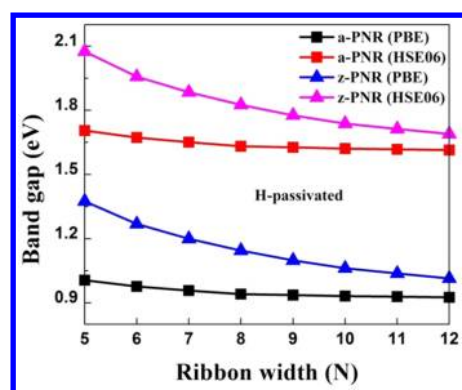
Figure 6. Variation of the bandgap of the edge H-passivated PNRs versus their width N ($5 \leq N \leq 12$).

energy E_{c1} is defined as $E_{c1} = (nE_P - E_{P_n})/n$; for the edge H-passivated PNRs, the cohesive energy E_{c2} is defined as $E_{c2} = (nE_P + mE_H - E_{P_nH_m})/(n + m)$, where E_P and E_H are the total energy of a single P and H atoms, respectively; E_{P_n} is the total energy of the edge-unpassivated PNR, and $E_{P_nH_m}$ is the total energy of the edge H-passivated PNR; and n and m are the number of P and H atoms in the PNR supercell, respectively. PNRs with greater cohesive energy per atom are energetically more stable. The cohesive energy of PNRs increases gradually with increasing ribbon width. Clearly, the cohesive energy of zigzag PNRs is greater than that of armchair PNRs with the same ribbon width. As a comparison, the computed cohesive energy per atom of bulk black phosphorus is 3.79 eV. Born–Oppenheimer molecular dynamics (BOMD) simulations are also carried out to examine thermal stabilities of the PNRs. The 7-armchair and 7-zigzag PNRs with or without H-passivation at an elevated temperature (600 K) and 1 atm pressure are performed. As shown in Figure S9 of Supporting Information, after 8 ps of simulation, the structures of armchair PNRs show little structure changes. Some edge reconstruction can be seen for zigzag PNRs without passivation (Figure S9c). However, with the H-passivation, the edge reconstruction is not seen (Figure S9d), indicating that the edges of the zigzag PNRs are much more stable with the passivation.

One-Dimensional Single-Walled Phosphorus Nanotubes. As shown in Figure 7, a SW-PNT can be viewed as rolling up a phosphorene monolayer. A previous study reported
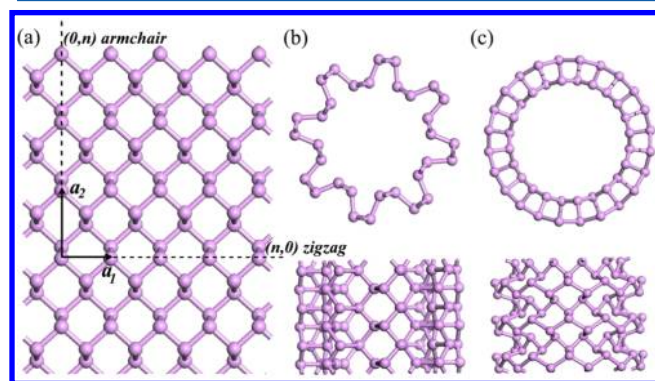

Figure 7. Schemtic plots of SW-PNTs which can be viewed as rolling up a phosphorene sheet following the roll-up vector $\mathbf{R} = n_1\mathbf{a}_1 + n_2\mathbf{a}_2$. Top and side views of a structure of (b) armchair and (c) zigzag SW-PNTs.

a SW-PNT constructed by rolling up a flat phosphorus sheet with graphene-like structure.[39] Here, a monolayer phosphorene with ridged structure is directly rolled up to construct the SW-PNT. The conformation of any specific SW-PNT can be described with a pair of integer indexes (n_1, n_2) that defines a rollup vector $\mathbf{R} = n_1\mathbf{a}_1 + n_2\mathbf{a}_2$ (see Figure 7). Two types of SW-PNTs are considered in this study, zigzag $(n_1, 0)$ and armchair $(0, n_2)$. A number of small diameter SW-PNTs with diameters ranging from 12 to 19 Å are investigated.

As shown in Table 1, for armchair PNTs (a-PNTs), the optimized unit-cell length L_c in the axial direction is 3.30 Å,

Table 1. Diameter of SW-PNTs D, Unit-Cell Length L_c in the Axial Direction, Computed Bandgap E_{g1} Based on PBE Functional, Bandgap E_{g2} Based on HSE06 Functional, and the Strain Energy E_S

SW-PNT	D (Å)	L_c (Å)	E_{g1} (eV)	E_{g2} (eV)	E_S (eV/atom)
(0, 8)	12.50	3.30	0.28	0.76	0.06
(0, 9)	13.86	3.30	0.36	0.91	0.04
(0, 10)	15.24	3.30	0.44	1.01	0.03
(0, 11)	16.66	3.30	0.51	1.10	0.02
(0, 12)	18.12	3.30	0.56	1.16	0.02
(0, 13)	19.48	3.30	0.61	1.22	0.01
(12, 0)	14.28	4.13	0.10	0.47	0.23
(13, 0)	15.23	4.17	0.13	0.57	0.20
(14, 0)	16.25	4.20	0.14	0.62	0.18
(15, 0)	17.16	4.30	0.22	0.74	0.16
(16, 0)	18.10	4.40	0.31	0.92	0.14
(17, 0)	18.98	4.48	0.35	0.99	0.13

independent to the diameter of a-PNTs. However, for zigzag PNTs (z-PNTs), the optimized unit-cell length L_c gradually increases with D, from $L_c = 4.13$ Å for (12, 0) to $L_c = 4.48$ Å for (17, 0). The calculated strain energy per atom, defined as the cohesive energy difference between the PNT and a perfect phosphorene monolayer, is also shown in Table 1. The strain energy per atom can be used to evaluate relative stabilities of the PNTs. For both armchair and zigzag SW-PNTs, as expected, the strain energy decreases with increasing D. However, the a-PNTs give rise to much smaller strain energies compared to that of the z-PNTs with nearly the same D, indicating that the a-PNTs are energetically more favorable than z-PNTs. Our BOMD simulation also supports this conclusion. The z-PNT (12,0) is disrupted even at room temperature (300 K) after 0.3 ps of simulation, indicating low stabilites of the narrower zigzag phosphorene nanotube. As shown in Figure S9 of Supporting Information, the structure of the a-PNT (0,8) is still intact at 600 K after 8 ps of simulation but shows some deformation from the circular shape (see top view in Figure S9e). At 400 K, the overall structure of the a-PNT (0,8) is well kept after 8 ps simulation.

Importantly, both a-PNTs and z-PNTs are semiconductors with their bandgaps increasing with D. For armchair SW-PNTs, the bandgap increases from 0.28 eV (0.76 eV based on HSE06) for $D = 12.50$ Å to 0.61 eV (1.22 eV based on HSE06) for $D = 19.48$ Å. For zigzag SW-PNTs, the bandgap increases from 0.1 eV (0.47 eV based on HSE06) for $D = 14.28$ Å to 0.3 eV (0.99 eV based on HSE06) for $D = 18.98$ Å. The computed electronic structures of armchair (0, 8) and zigzag (12, 0) SW-PNTs are shown in Figure 8. The armchair (0, 8) SW-PNT has a direct bandgap with its VBM and CBM being located at the Γ point. As shown in Figure 8a, the VBM manifests a bonding
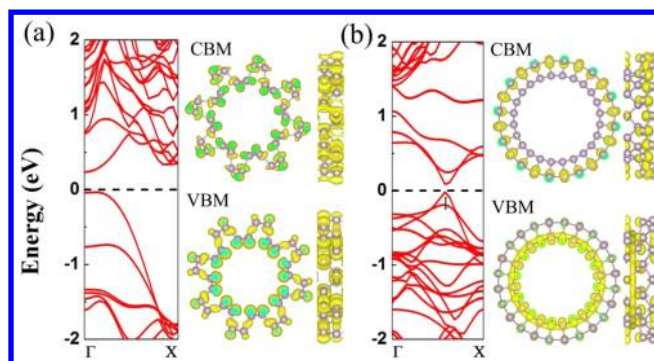
Figure 8. Computed band structure (PBE) and partial charge density distribution corresponding to the VBM and CBM of (a) armchair (0, 8) and (b) zigzag (12, 0) SW-PNTs. The isosurface value is 0.001 e/bohr^3. The Fermi level is set to zero.

character between the inner and outer P atoms, while the CBM exhibits a diffusive state of the outer or inner P−P bond along the axis. The zigzag (12, 0) SW-PNT has a direct bandgap with the CBM and VBM located at the I point (see Figure 8b). The VBM manifests mainly the bonding state between inner atoms, while the CBM is mainly due to isolated p_z states of outer atoms.

Again, electronic properties of the SW-PNTs can be modified through either elongation or compression of the nanotubes in the axial direction. For armchair (0, 8) SW-PNT, it undergoes a direct-to-indirect bandgap transition under a critical tensile strain (see Figure S10 of Supporting Information). The CBM is still located at the Γ point, while the VBM is shifted along the Γ−X line. As shown in Figure 9a, the bandgap increases up to
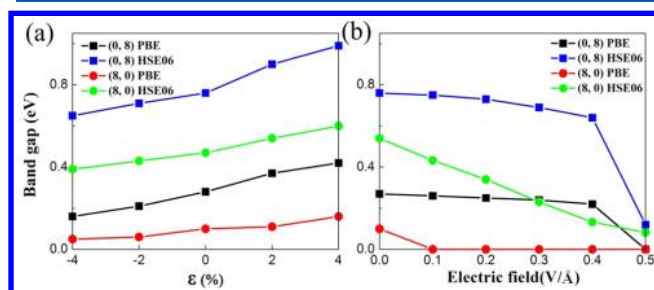

Figure 9. Computed bandgaps (PBE and HSE06) of armchair (0, 8) and zigzag (12, 0) SW-PNTs versus (a) tensile strain, ranging from −4% to 4%, where "−" represents compression and "+" indicates expansion; and (b) the transverse electric field, ranging from 0.1 to 0.5 V/Å.

0.42 eV (0.99 eV for HSE06) with increasing expansion strain up to 4%. The bandgap decreases gradually with compression strain down to −4%, where the corresponding bandgap is 0.17 eV (or 0.65 eV based on HSE06). The PBE results indicate that the bandgap is enlarged by ∼0.25 eV with the strain changing from −4% to 4%, while the HSE06 results show the same trend with the bandgap enlarged by 0.34 eV. As shown in Figure S10 of Supporting Information, the upshift of the CBM for about 0.19 eV with the strain changing from −4% to 4% is the main reason for the bandgap enlargement. Because the CBM is mainly contributed by the outer P−P bond along the axial direction, any appreciable deformation along the axial direction would significantly affect bandgaps of armchair SW-PNTs. For zigzag (12, 0) SW-PNT, its bandgap also increases with increasing tensile strain. However, both the CBM and VBM are

shifted downward under the strain while the VBM is shifted downward more than the CBM, thereby leading to a net increase in the bandgap (see Figure S11 of Supporting Information).

Figure 9b shows that when the armchair (0, 8) PNT is subjected to a transverse electric field, its bandgap decreases with increasing the field strength. A semiconductor-to-metal transition occurs when the electric field reaches 0.5 V/Å. For zigzag (8, 0) PNT, the bandgap also decreases with increasing field strength, while the semiconductor-to-metal transition occurs when the field reaches 0.1 V/Å. Moreover, HSE06 results confirm the same trend on the field-dependent bandgap. Again, the gap modulation can be understood through the Stark effect. Overall, our calculations show that either the tensile strain or transverse electric field can significantly affect bandgaps of PNTs, regardless of PNT chirality.

Multilayer Phosphorene Sheets. It is known that the bulk black phosphorus exhibits the AB stacking in packed layers. A recent theoretical study demonstrates that AB stacking is the most stable configuration for phosphorene bilayer.[40] Hence, we also consider the AB stacking for multilayer phosphorene sheets (see Figure S12 of Supporting Information). The optimized cell parameters and interlayer distance for 1−4 layer phosphorene sheets are listed in Table S1 of Supporting Information, which are found to be in agreement with previous studies.[13] Computed electronic structures of 1−4 layer phosphorene sheets, based on the PBE calculations, are shown in Figure 10. The phosphorene monolayer is a
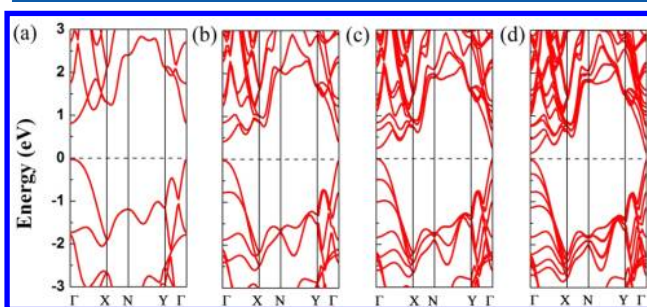

Figure 10. Computed band structures (PBE) of (a) monolayer, (b) bilayer, (c) trilayer, and (d) 4-layer phosphorene sheets. The Fermi level is set to zero.

semiconductor with a direct bandgap of 0.84 eV at the Γ point (Figure 10a), consistent with previous results.[17] Bilayer, trilayer, and 4-layer phosphorene sheets are also semiconductors with a direct bandgap of 0.44, 0.25, and 0.16 eV, respectively. The bandgaps of multilayer phosphorene sheets decrease with increasing the number of layers. Calculations based on the HSE06 functional also confirm this trend (see Figure S13 of Supporting Information), giving direct bandgaps of 1.51, 1.04, 0.81, and 0.70 eV for monolayer, bilayer, trilayer, and 4-layer phosphorene sheets, respectively.

As shown in Figure 11a, when a phosphorene monolayer is subjected to a vertical electric field, its bandgap exhibits little change. However, for a phosphorene bilayer, its bandgap decreases slightly upon application of the vertical electric field. With an increase in the number of layers, the bandgap reduction due to the vertical electric field becomes more significant. Such a layer-dependent bandgap reduction due to the vertical electric field can be understood by the Stark effect. The difference in electric potential among different phosphor-
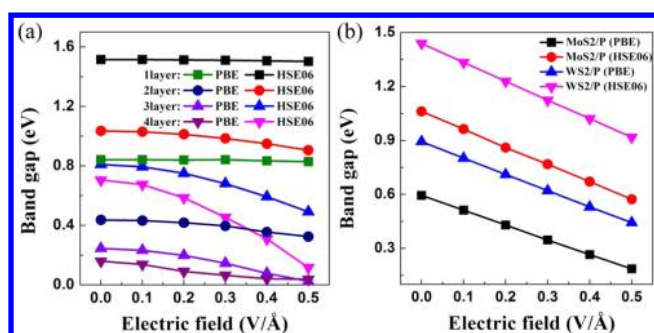
Figure 11. Vertical electric-field-dependent bandgap (PBE and HSE06) for (a) multilayer phosphorene sheets and (b) TMDC/phosphorene heterobilayers.

ene layers can be induced by the vertical electric field.[23] As a result, the bands belonging to different phosphorene layers are further split by the vertical electric field. The splitting is proportional to the number of layers as well as the strength of the vertical electric field, thereby resulting in stronger bandgap modulation for thicker phosphorene sheets.

Heterobilayers of Phosphorene and TMDC Monolayer. A recent experiment demonstrated successful preparation of a CMOS inverter which combines a phosphorene p-type MOS transistor with a MoS$_2$ n-type MOS transistor. Here, electronic properties of MoS$_2$/phosphorene and WS$_2$/phosphorene heterobilayers (i.e., one n-type and one p-type) are computed, as shown in Figure 12.
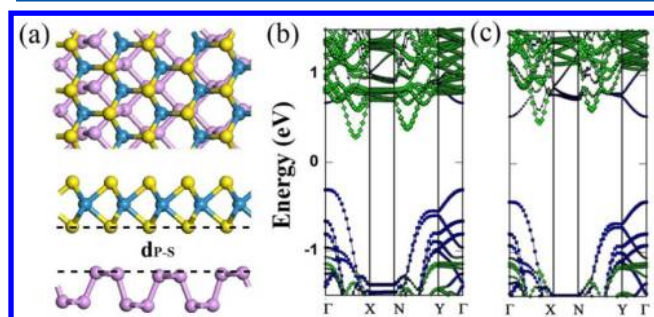

Figure 12. (a) Top and side views of the optimized MoS$_2$ (or WS$_2$)/phosphorene heterobilayer structure. (b) Computed band structures (PBE) of (b) MoS$_2$/phosphorene and (c) WS$_2$/phosphorene heterobilayers. Blue, yellow, and purple spheres represent Mo (or W), S, and P atoms, respectively. The d_{P-S} denotes the interlayer height difference between P and S atoms. The green lines mark contribution from MoS$_2$ or WS$_2$ monolayer, while the blue lines mark contribution from the phosphorene monolayer. The Fermi level is set to zero.

The distance between WS$_2$ and phosphorene monolayer is 3.30 Å, and the distance between MoS$_2$ and phosphorene monolayer is 3.21 Å, suggesting weak van der Waals interaction between MoS$_2$ (WS$_2$) and phosphorene layers. We also compute the binding energy between the two layers. Here, the binding energy is defined as $E_{BE} = (E_P + E_{MoS_2(WS_2)} - E_{MoS_2(WS_2)/P})/n$, where E_P, $E_{MoS_2(WS_2)}$, and $E_{MoS_2(WS_2)/P}$ are the total energy of a phosphorene monolayer, a MoS$_2$ (WS$_2$) monolayer, and a MoS$_2$(WS$_2$)/phosphorene heterobilayer, respectively; n is the total number of atoms per supercell. The computed binding energies of MoS$_2$/phosphorene and WS$_2$/phosphorene heterobilayers are 36 and 35 meV per atom,

respectively, again consistent with weak van der Waals interaction between MoS$_2$ (WS$_2$) and phosphorene layers.

Figure 12b,c shows that both MoS$_2$/phosphorene and WS$_2$/phosphorene heterobilayers are semiconductors with an indirect bandgap of 0.59 and 0.89 eV (PBE), respectively. Both MoS$_2$/phosphorene and WS$_2$/phosphorene heterobilayers exhibit type II alignment, which may be advantageous for the separation of electron−hole pairs. The partial density of state (PDOS) analysis suggests that the VBM is mainly contributed by the p orbital of P atoms and that the CBM is mainly contributed by the d orbital of Mo (or W) atoms (Figure S14 of Supporting Information). HSE06 calculations give indirect bandgaps of 1.06 and 1.44 eV for MoS$_2$/phosphorene and WS$_2$/phosphorene heterobilayers, respectively. Although the external electric field has little effect on either the monolayer phosphorene or monolayer TMDC, it has significant effect on the heterobilayer. As shown in Figure 11b, a vertical electric field can significantly reduce the bandgap of TMDC/phosphorene heterobilayers. Bader charge anlaysis suggests that the charge transfer between TMDC and phosphorene increases gradually with the electric field (see Table S2 of Supporting Information).

Finally, we note that bilayer phosphorene has been predicted by us to be a good candidate as solar cell donor material with the monolayer MoS$_2$ as an acceptor.[40] On the basis of HSE06 computation, the band offsets between monolayer, bilayer, trilayer, 4-layer phosphorene, and monolayer MoS$_2$ are given in Figure 13a; all exhibit a type II alignment. Under the assumption of 100% external quantum efficiency (EQE), the upper limit of the power conversion efficiency (PCE) can be estimated by using the following formula:

$$\eta = \frac{J_{SC} V_{OC} \beta_{FF}}{P_{solar}} = \frac{0.65(E_g^d - \Delta E_C - 0.3) \int_{E_g}^{\infty} \frac{P(\hbar\varpi)}{\hbar\varpi} \, d(\hbar\varpi)}{\int_0^{\infty} P(\hbar\varpi) \, d(\hbar\varpi)}$$

where 0.65 is the band-fill factor (FF), E_g^d is the bandgap of the donor, the $(E_g^d - \Delta E_C - 0.3)$ term is an estimation of the maximum open circuit voltage V_{OC} and $P(\hbar\varpi)$ is the AM1.5 solar energy flux (expressed in Wm^{-2}eV^{-1}) at the photon energy $\hbar\varpi$. The integral in the numerator is the short circuit current J_{SC} under the limit of 100% EQE, and the integral in the denominator is the AM1.5 solar flux. As shown in Figure 13b, with fewer phosphorene layers, the PCE of solar cell systems consisting of multilayer phosphorene and a monolayer MoS$_2$ increases gradually from 11.5% to 17.5%. The monolayer phosphorene combined with monolayer MoS$_2$ would yield the maximum PCE around 17.5%.

■ CONCLUSIONS

In conclusion, we have performed a first-principles study of structural and electronic properties of PNRs, SW-PNTs, multilayers, and 2D TMDC/phosphorene heterobilayers, as well as tunability of their bandgaps by applying either a tensile strain or an external electric field. Our calculations show that the edge-unpassivated zigzag PNRs are metallic, while the edge-unpassivated armchair PNRs are semiconducting with indirect bandgaps. With hydrogen-passivated edges, z-PNRs become semiconductors with nearly direct bandgaps while a-PNRs become semiconductors with direct bandgaps. All armchair and zigzag SW-PNTs are semiconducting with direct bandgaps. The bandgaps of edge-unpassivated armchair PNRs, edge H-passivated PNRs, and SW-PNTs can be modulated by either
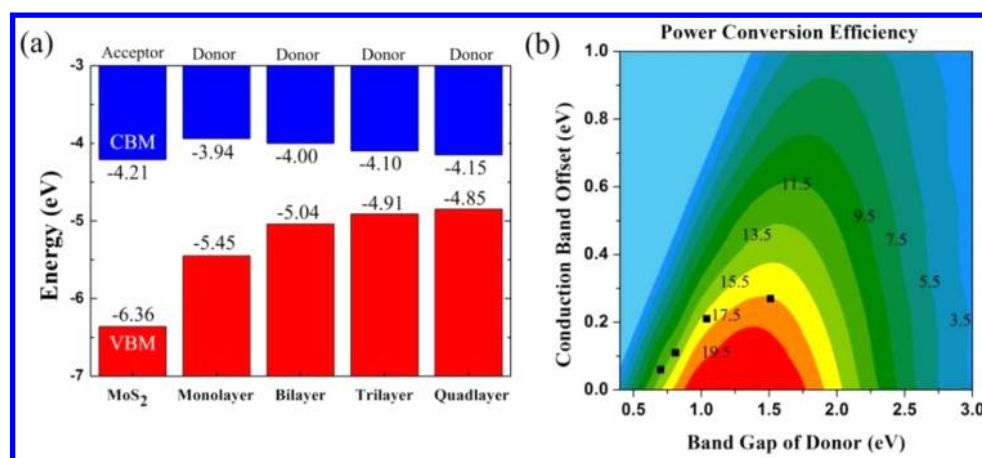
Figure 13. (a) Computed band alignment between monolayer MoS_2 and monolayer, bilayer, trilayer, or 4-layer phosphorene based on HSE06 computations. The vacuum level is set to zero. (b) Computed PCE contour as a function of the donor bandgap and conduction band offset.

tensile strain or transverse electric field. All multilayer phosphorene sheets are semiconducting with their bandgap decreasing with more stacked layers. Moreover, a vertical electric field can modulate bandgaps of multilayer phosphorene sheets as well as those of 2D TMDC/phosphorene heterobilayers. Our calculations have shown that the PCE of solar cell systems consisting of a multilayer phosphorene and a monolayer MoS_2 increases gradually from 11.5% to 17.5% with a decrease in the number of phosphorene layers. The combined monolayer phosphorene with monolayer MoS_2 could yield theoretical maximum PCE around 17.5%. These novel electronic properties of low-dimensional (1D and 2D) phosphorene nanostructures, in conjuction with their remarkable strain enegineering and electric field effects in tuning the bandgaps, suggest that phosphorene is a promising candidate for future nanoelectronic and optoelectronic applications.

COMPUTATIONAL DETAILS

In this work, all calculations are performed within the framework of spin-polarized density functional theory (DFT), implemented in the Vienna ab initio simulation package (VASP).[41,42] The generalized gradient approximation (GGA) in the form of the Perdew–Burke–Ernzerhof (PBE) functional and projector augmented wave (PAW) potentials are used.[43−45] Effect of van der Waals (vdW) interaction is accounted for by using a dispersion-corrected DFT method (optB88-vdW functional),[46,47] which has been proven reliable for multilayer phosphorene systems.[13] For bulk black phosphorus, the optB88-vdW predicts the lattice constants a = 4.47 Å, b = 3.34 Å, and c = 10.69 Å, in good agreement with experimental values[48] (a = 4.38 Å, b = 3.31 Å, and c = 10.48 Å). With the optB88-vdW optimized structure, the computed HSE06 bandgap of the bulk black phosphorus is 0.38 eV, in very good agreement with the experimental values of 0.31−0.35 eV.[49−52] More specifically, a 1×1 unit cell is adopted for all calculations except for MoS_2/phosphorene and WS_2/phosphorene heterobilayers for which the 1×5 MoS_2 or WS_2 supercell that nearly matches the 1×6 phosphorene supercell (with the lattice mismatch less than 5%) is adopted. The vacuum size is larger than 15 Å between two adjacent images. An energy cutoff of 500 eV is adopted for the plane-wave expansion of the electronic wave function. Geometric structures are relaxed until the force on each atom is less than 0.01 eV/Å and the energy convergence criteria of 1×10^{-5} eV are met. For each system,

the unit cell is optimized to obtain the lattice parameters corresponding to the lowest energy. Uniaxial tensile strain along the direction of nanoribbon (or nanotube axis) is applied. Effects of transverse electric field along the lateral direction of the nanoribbon (or nanotube) are investigated. The uniform electric field is handled in VASP by adding an artificial dipole sheet in the supercell.[53] The geometries are kept fixed when applying the external electric field to avoid the geometric contribution to the electronic structures. Because the DFT/PBE method tends to underestimate bandgap of semiconductors, the screened hybrid HSE06 method is also used to examine the band structures.[54] The BOMD simulations are performed using the CASTEP package.[55,56] The supercells are three times the unit cell used for band-structure computations. For the DFT computation, PBE functional and ultrasoft pseudopotential are selected. The energy cutoff is 160 eV. The BOMD simulations are carried out in the constant-temperature and constant-pressure ensemble. The temperature and pressure (1 atm) are controlled using the Nosé−Hoover method[57] and the Anderson−Hoover method,[58] respectively. The time step is 2 fs. Each independent BOMD simulation lasts 8 ps.

ASSOCIATED CONTENT

Ⓢ Supporting Information

Computed band structures (PBE) of the edge-unpassivated zigzag and armchair PNRs; partial charge density distribution corresponding α and β bands at the Γ point for the edge-unpassivated 8-zigzag PNR; band structures (PBE) of the edge-unpassivated 8-armchair PNR at the strain of −4% and 4%; band structures (PBE) and partial charge density of the edge-unpassivated 8-armchair PNR at the external electric field of 0 V/Å and 0.1 V/Å; the computed band gaps of the edge H-passivated 7-armchair PNR and 7-zigzag PNR versus tensile strain and in-plane transverse electric field; band structures (PBE) of a-PNT (0, 8) at the strain of −4% and 4%; band structures (PBE) of z-PNT (12, 0) at the strain of −4% and 4%; cohesive energy per atom of the edge-unpassivated PNRs versus ribbon width ($5 \leq N \leq 12$); cohesive energy per atom of the edge H-passivated PNRs versus ribbon width ($5 \leq N \leq 12$); snapshots of the edge-unpassivated 7-armchair PNR, the edge H-passivated 7-armchair PNR, the edge-unpassivated 7-zigzag PNR, the edge H-passivated 7-zigzag PNR, and armchair PNT (0, 8) at 600 K, and the armchair PNT (0, 8) at 400 K in the BOMD simulations at time 8 ps; geometric structure of

14057

dx.doi.org/10.1021/jp505257g | J. Phys. Chem. C 2014, 118, 14051−14059

multilayer phosphorene; computed band structures (based on HSE06) of multilayer phosphorene; partial density of states (PDOS) of MoS_2/phosphorene and WS_2/phosphorene heterobilayers; cell parameter a_1 and a_2 of multilayer phosphorene and the interlayer spacing between two adjacent phosphorene layers d_{int}; charge transfer between TMDC and phosphorene layers with and without the electric field. This material is available free of charge via the Internet at http://pubs.acs.org.

■ AUTHOR INFORMATION

Corresponding Authors
*E-mail: xzeng1@unl.edu.
*E-mail: xjwu@ustc.edu.cn.
Author Contributions
[⊥]These authors (H.G. and N.L.) contributed equally to this work.

Notes
The authors declare no competing financial interest.

■ ACKNOWLEDGMENTS

■ REFERENCES

(1) Novoselov, K. S.; Geim, A. K.; Morozov, S. V.; Jiang, D.; Zhang, Y.; Dubonos, S. V.; Grigorieva, I. V.; Firsov, A. A. Electric Field Effect in Atomically Thin Carbon Films. *Science* **2004**, *306*, 666−669.

(2) Lu, N.; Li, Z.; Yang, J. Electronic Structure Engineering via On-plane Chemical Functionalization: A Comparison Study on Two-Dimensional Polysilane and Graphane. *J. Phys. Chem. C* **2009**, *113*, 16741−16746.

(3) Guo, H.; Zhao, Y.; Lu, N.; Kan, E.; Zeng, X. C.; Wu, X.; Yang, J. Tunable Magnetism in a Nonmetal-Substituted ZnO Monolayer: A First-Principles Study. *J. Phys. Chem. C* **2012**, *116*, 11336−11342.

(4) Dai, J.; Wu, X.; Yang, J.; Zeng, X. C. Unusual Metallic Microporous Boron Nitride Networks. *J. Phys. Chem. Lett.* **2013**, *4*, 3484−3488.

(5) Fuhrer, M. S.; Hone, J. Measurement of Mobility in Dual-gated MoS_2 Transistors. *Nat. Nanotechnol.* **2013**, *8*, 146−147.

(6) Radisavljevic, B.; Kis, A. Reply to 'Measurement of Mobility in Dual-gated MoS_2 Transistors'. *Nat. Nanotechnol.* **2013**, *8*, 147−148.

(7) Appalakondaiah, S.; Vaitheeswaran, G.; Lebegue, S.; Christensen, N. E.; Svane, A. Effect of Van der Waals Interactions on the Structural and Elastic Properties of Black Phosphorus. *Phys. Rev. B: Condens. Matter Mater. Phys.* **2012**, *86*, 035105.

(8) Buscema, M.; Groenendijk, D. J.; Blanter, S. I.; Steele, G. A.; van der Zant, H. S.; Castellanos-Gomez, A.. Fast and Broadband Photoresponse of Few-layer Black Phosphorus Field-effect Transistors. 2014, arXiv:1403.0565. *arXiv preprint*. http://arxiv.org/abs/1403.0565.

(9) Castellanos-Gomez, A.; Vicarelli, L.; Prada, E.; Island, J. O.; Narasimha-Acharya, K.; Blanter, S. I.; Groenendijk, D. J.; Buscema, M.; Steele, G. A.; Alvarez, J. Isolation and Characterization of Few-layer Black Phosphorus. 2014, arXiv:1403.0499. *arXiv preprint*. http://arxiv.org/abs/1403.0499.

(10) Fei, R.; Yang, L. Strain-Engineering Anisotropic Electrical Conductance of Phosphorene. 2014, arXiv:1403.1003. *arXiv preprint*. http://arxiv.org/abs/1403.1003.

(11) Koenig, S. P.; Doganov, R. A.; Schmidt, H.; Neto, A.; Oezyilmaz, B. Electric Field Effect in Ultrathin Black Phosphorus. 2014, arXiv:1402.5718. *arXiv preprint*. http://arxiv.org/abs/1402.5718.

(12) Li, L.; Yu, Y.; Ye, G. J.; Ge, Q.; Ou, X.; Wu, H.; Feng, D.; Chen, X. H.; Zhang, Y. Black Phosphorus Field-effect Transistors. *Nat. Nano* **2014**, *9*, 372−377.

(13) Qiao, J.; Kong, X.; Hu, Z.-X.; Yang, F.; Ji, W. Few-layer Black Phosphorus: Emerging Direct Band Gap Semiconductor with High Carrier Mobility. 2014, arXiv:1401.5045. *arXiv preprint*. http://arxiv.org/abs/1401.5045.

(14) Rodin, A.; Carvalho, A.; Neto, A. Strain-induced Gap Modification in Black Phosphorus. 2014, arXiv:1401.1801. *arXiv preprint*. http://arxiv.org/abs/1401.1801.

(15) Tran, V.; Soklaski, R.; Liang, Y.; Yang, L. Layer-Controlled Band Gap and Anisotropic Excitons in Phosphorene. 2014, arXiv:1402.4192v1. *arXiv preprint*. http://arxiv.org/abs/1402.4192v1.

(16) Xia, F.; Wang, H.; Jia, Y. Rediscovering Black Phosphorus: A Unique Anisotropic 2D Material for Optoelectronics and Electronics. 2014, arXiv:1402.0270. *arXiv preprint*. http://arxiv.org/abs/1402.0270.

(17) Liu, H.; Neal, A. T.; Zhu, Z.; Luo, Z.; Xu, X.; Tománek, D.; Ye, P. D. Phosphorene: An Unexplored 2D Semiconductor with a High Hole Mobility. *ACS Nano* **2014**, *8*, 4033−4041.

(18) Wu, X.; Xu, Z.; Zeng, X. C. Single-walled $MoTe_2$ nanotubes. *Nano Lett.* **2007**, *7*, 2987−2992.

(19) Li, Y.; Zhou, Z.; Zhang, S.; Chen, Z. MoS_2 Nanoribbons: High Stability and Unusual Electronic and Magnetic Properties. *J. Am. Chem. Soc.* **2008**, *130*, 16739−16744.

(20) Kang, J.; Wu, F.; Li, J. Modulating the Bandgaps of Graphdiyne Nanoribbons by Transverse Electric Fields. *J. Phys.: Condens. Matter* **2012**, *24*, 165301.

(21) Geim, A.; Grigorieva, I. Van der Waals Heterostructures. *Nature (London, U.K.)* **2013**, *499*, 419−425.

(22) Ramasubramaniam, A.; Naveh, D.; Towe, E. Tunable Band Gaps in Bilayer Transition-Metal Dichalcogenides. *Phys. Rev. B: Condens. Matter Mater. Phys.* **2011**, *84*, 205325.

(23) Liu, Q.; Li, L.; Li, Y.; Gao, Z.; Chen, Z.; Lu, J. Tuning Electronic Structure of Bilayer MoS_2 by Vertical Electric Field: A First-Principles Investigation. *J. Phys. Chem. C* **2012**, *116*, 21556−21562.

(24) Kou, L.; Frauenheim, T.; Chen, C. Nanoscale Multilayer Transition-Metal Dichalcogenide Heterostructures: Band Gap Modulation by Interfacial Strain and Spontaneous Polarization. *J. Phys. Chem. Lett.* **2013**, *4*, 1730−1746.

(25) Lu, N.; Guo, H.; Li, L.; Dai, J.; Wang, L.; Mei, W.-N.; Wu, X.; Zeng, X. C. MoS_2/MX_2 Heterobilayers: Bandgap Engineering via Tensile Strain or External Electrical Field. *Nanoscale* **2014**, *6*, 2879−2886.

(26) Lu, N.; Guo, H.; Wang, L.; Wu, X.; Zeng, X. C. Van der Waals Trilayers and Superlattices: Modification of Electronic Structures of MoS_2 by Intercalation. *Nanoscale* **2014**, *6*, 4566−4571.

(27) Johari, P.; Shenoy, V. B. Tuning the Electronic Properties of Semiconducting Transition Metal Dichalcogenides by Applying Mechanical Strains. *ACS Nano* **2012**, *6*, 5449−5456.

(28) Ma, Y.; Dai, Y.; Guo, M.; Niu, C.; Zhu, Y.; Huang, B. Evidence of the Existence of Magnetism in Pristine VX_2 Monolayers (X= S, Se) and Their Strain-Induced Tunable Magnetic Properties. *ACS Nano* **2012**, *6*, 1695−1701.

(29) Yun, W. S.; Han, S.; Hong, S. C.; Kim, I. G.; Lee, J. Thickness and Strain Effects on Electronic Structures of Transition Metal Dichalcogenides: 2H-MX_2 Semiconductors (M= Mo, W; X= S, Se, Te). *Phys. Rev. B: Condens. Matter Mater. Phys.* **2012**, *85*, 033305.

(30) Zhou, Y.; Wang, Z.; Yang, P.; Zu, X.; Yang, L.; Sun, X.; Gao, F. Tensile Strain Switched Ferromagnetism in Layered NbS_2 and $NbSe_2$. *ACS Nano* **2012**, *6*, 9727−9736.

(31) Conley, H. J.; Wang, B.; Ziegler, J. I.; Haglund, R. F.; Pantelides, S. T.; Bolotin, K. I. Bandgap Engineering of Strained Monolayer and Bilayer MoS_2. *Nano Lett.* **2013**, *13*, 3626−3630.

(32) Hui, Y. Y.; Liu, X.; Jie, W.; Chan, N. Y.; Hao, J.; Hsu, Y.-T.; Li, L.-J.; Guo, W.; Lau, S. P. Exceptional Tunability of Band Energy in a

Compressively Strained Trilayer MoS$_2$ Sheet. *ACS Nano* **2013**, *7*, 7126−7131.

(33) Lu, A.; Zhang, R.; Lee, S. Stress-induced Band Gap Tuning in ⟨112⟩ Silicon Nanowires. *Appl. Phys. Lett.* **2007**, *91*, 263107.

(34) Zhang, Z.; Guo, W. Energy-gap Modulation of BN Ribbons by Transverse Electric Fields: First-principles Calculations. *Phys. Rev. B: Condens. Matter Mater. Phys.* **2008**, *77*, 075403.

(35) Zhang, C.; De Sarkar, A.; Zhang, R.-Q. Strain Induced Band Dispersion Engineering in Si Nanosheets. *J. Phys. Chem. C* **2011**, *115*, 23682−23687.

(36) Zhang, Z.; Guo, W.; Yakobson, B. I. Self-modulated Band Gap in Boron Nitride Nanoribbons and Hydrogenated Sheets. *Nanoscale* **2013**, *5*, 6381−6387.

(37) Bhattacharyya, S.; Singh, A. K. Semiconductor-metal Transition in Semiconducting Bilayer Sheets of Transition-metal Dichalcogenides. *Phys. Rev. B: Condens. Matter Mater. Phys.* **2012**, *86*, 075454.

(38) Guo, H.; Lu, N.; Wang, L.; Wu, X.; Zeng, X. C. Tuning Electronic and Magnetic Properties of Early Transition-Metal Dichalcogenides via Tensile Strain. *J. Phys. Chem. C* **2014**, *118*, 7242−7249.

(39) Seifert, G.; Hernández, E. Theoretical Prediction of Phosphorus Nanotubes. *Chem. Phys. Lett.* **2000**, *318*, 355−360.

(40) Dai, J.; Zeng, X. C. Bilayer Phosphorene: Effect of Stacking Order on Bandgap and Its Potential Applications in Thin-Film Solar Cells. *J. Phys. Chem. Lett.* **2014**, *5*, 1289−1293.

(41) Kresse, G.; Furthmüller, J. Efficient Iterative Schemes for Ab Initio Total-energy Calculations Using a Plane-wave Basis Set. *Phys. Rev. B: Condens. Matter Mater. Phys.* **1996**, *54*, 11169.

(42) Kresse, G.; Furthmüller, J. Efficiency of Ab Initio Total Energy Calculations for Metals and Semiconductors Using a Plane-wave Basis Set. *Comput. Mater. Sci.* **1996**, *6*, 15−50.

(43) Kresse, G.; Hafner, J. Ab Initio Molecular Dynamics for Liquid Metals. *Phys. Rev. B: Condens. Matter Mater. Phys.* **1993**, *47*, 558.

(44) Kresse, G.; Joubert, D. From Ultrasoft Pseudopotentials to the Projector Augmented-wave Method. *Phys. Rev. B: Condens. Matter Mater. Phys.* **1999**, *59*, 1758.

(45) Perdew, J. P.; Burke, K.; Ernzerhof, M. Generalized Gradient Approximation Made Simple. *Phys. Rev. Lett.* **1996**, *77*, 3865.

(46) Klimeš, J.; Bowler, D. R.; Michaelides, A. Chemical Accuracy for the Van der Waals Density Functional. *J. Phys.: Condens. Matter* **2010**, *22*, 022201.

(47) Klimeš, J.; Bowler, D. R.; Michaelides, A. Van der Waals Density Functionals Applied to Solids. *Phys. Rev. B: Condens. Matter Mater. Phys.* **2011**, *83*, 195131.

(48) Brown, A.; Rundqvist, S. Refinement of the Crystal Structure of Black Phosphorus. *Acta Crystallogr.* **1965**, *19*, 684−685.

(49) Keyes, R. W. The Electrical Properties of Black Phosphorus. *Phys. Rev.* **1953**, *92*, 580.

(50) Maruyama, Y.; Suzuki, S.; Kobayashi, K.; Tanuma, S. Synthesis and Some Properties of Black Phosphorus Single Crystals. *Physica B+C (Amsterdam)* **1981**, *105*, 99−102.

(51) Akahama, Y.; Endo, S.; Narita, S.-i. Electrical Properties of Black Phosphorus Single Crystals. *J. Phys. Soc. Jpn.* **1983**, *52*, 2148−2155.

(52) Warschauer, D. Electrical and Optical Properties of Crystalline Black Phosphorus. *J. Appl. Phys.* **1963**, *34*, 1853−1860.

(53) Neugebauer, J.; Scheffler, M. Adsorbate-substrate and Adsorbate-adsorbate Interactions of Na and K Adlayers on Al(111). *Phys. Rev. B: Condens. Matter Mater. Phys.* **1992**, *46*, 16067−16080.

(54) Heyd, J.; Scuseria, G. E.; Ernzerhof, M. Erratum: "Hybrid Functionals Based on a Screened Coulomb Potential" [J. Chem. Phys. 118, 8207 (2003)]. *J. Chem. Phys.* **2006**, *124*, 219906.

(55) Segall, M.; Lindan, P. J.; Probert, M.; Pickard, C.; Hasnip, P.; Clark, S.; Payne, M. First-Principles Simulation: Ideas, Illustrations and the CASTEP Code. *J. Phys.: Condens. Matter* **2002**, *14*, 2717.

(56) Clark, S. J.; Segall, M. D.; Pickard, C. J.; Hasnip, P. J.; Probert, M. I.; Refson, K.; Payne, M. C. First Principles Methods Using CASTEP. *Z. Kristallogr.—Cryst. Mater.* **2005**, *220*, 567−570.

(57) Nosé, S. A Molecular Dynamics Method for Simulations in the Canonical Ensemble. *Mol. Phys.* **1984**, *52*, 255−268.

(58) Andersen, H. C. Molecular Dynamics Simulations at Constant Pressure and/or Temperature. *J. Chem. Phys.* **1980**, *72*, 2384−2393.